Electronic Supplementary Information (ESI) for Environmental Science: Nano.

Anatase TiO$_2$ nanomaterials are much more effective in enhancing hydrolysis of organophosphorus compounds than their rutile counterparts

Tong Li [1,2], Yiting Ju [1], Tingting Du [1], Chuanjia Jiang [2,*], Tong Zhang [2,*], Wei Chen [2,*]

[1] Information Materials and Intelligent Sensing Laboratory of Anhui Province, Institutes of Physical Science and Information Technology, Anhui University, Hefei, 230601, China

[2] College of Environmental Science and Engineering, Ministry of Education Key Laboratory of Pollution Processes and Environmental Criteria, Tianjin Key Laboratory of Environmental Remediation and Pollution Control, Nankai University, Tianjin 300350, China

* Corresponding authors: Chuanjia Jiang (E-mail: jiangcj@nankai.edu.cn); Tong Zhang (E-mail: zhangtong@nankai.edu.cn); Wei Chen (Tel/Fax: + 86 22 66229516; E-mail: chenwei@nankai.edu.cn).

S1. Chemicals and reagents

The 4-nitrophenyl phosphate (pNPP) disodium hexahydrate was purchased from Sigma-Aldrich (St. Louis, USA). The commercial nanoparticulate TiO_2 (P25) was purchased from Degussa Company (Frankfurt, Germany). Titanium butoxide ($C_{16}H_{36}O_4Ti$), titanium isopropoxide ($C_{12}H_{28}O_4Ti$), glycolic acid ($C_2H_4O_3$) and hydrofluoric acid (HF, 40%) were purchased from Aladdin Co. Ltd (Shanghai, China). Potassium hydroxide (KOH), sodium acetate (CH_3COONa), acetic acid (CH_3COOH), sodium hydroxide (NaOH), sodium chloride (NaCl), hydrochloric acid (HCl), sodium fluoride (NaF), sodium azide (NaN_3) and ethyl alcohol absolute were obtained from Sinopharm Chemical Reagent Co. Ltd (Shanghai, China). All chemicals were analytical grade and used without further purification. Ultrapure water was used in all experiments.

S2. Preparation of TiO_2 nanomaterials

The anatase TiO_2 nanomaterial with predominantly exposed {101} crystal facets was prepared using a two-step hydrothermal method.[1] In the first step, 1 g of P25 powder was added to 70 mL of KOH solution (10 M) in a 100-mL Teflon autoclave with magnetic stirring, and then the autoclave was kept at 200 °C for 48 h. The precipitates were washed with ultrapure water and dried in an oven at 60 °C. In the second step, the prepared powder (70 mg) was dispersed in 70 mL of ultrapure water and hydrothermally treated in a 100-mL Teflon autoclave at 170 °C for 24 h. The white precipitates were collected via centrifugation and finally dried at 100 °C. The sample was denoted as Ana_101.

The anatase TiO_2 nanomaterial with predominantly exposed {001} crystal facets was synthesized using a previously reported solvothermal method.[2] Briefly, 10 mL of titanium butoxide and 1.6 mL of hydrofluoric acid (40%) were mixed in a 50-mL Teflon autoclave, and

heated at 200 °C for 24 h. Then, the white precipitates were collected by centrifugation and repeatedly washed with ultrapure water and absolute ethanol. Next, the prepared powder was soaked in a NaOH (0.1 M) solution overnight to remove fluoride ions, followed by rinsing with ultrapure water. Finally, the white precipitates were collected via centrifugation and dried at 80 °C. The sample was denoted as Ana_001.

The rutile nanorods with predominantly exposed {110} facets were prepared by a previously reported hydrothermal method.[3] 6 mL of HCl (36.5 %) and 15 mL of titanium isopropoxide were mixed in a 100-mL Teflon autoclave and then kept at 180 °C for 36 h. After the autoclave was cooled to room temperature, the white precipitate was separated by centrifugation and washed several times with NaOH (0.5 M) solution and then with ultrapure water until the filtrate was neutral. The final products were dried in an oven at 80 °C overnight. The sample was denoted as Rut_110.

The rutile nanomaterial with a greater proportion of {111} facets was prepared according to a previous report.[4] First, 10 mL of titanium butoxide was added dropwise to 300 mL of glycolic acid solution (1.0 M) under stirring. The resulting white suspension was then heated to 90 °C for 30 min to produce a colorless and transparent precursor solution. Subsequently, 30 mL of the transparent solution and 3.0 mL of NaF solution (0.60 M) were mixed in a 50-mL Teflon autoclave and then heated at 180 °C for 12 h. After the autoclave was cooled to room temperature, the white precipitates were separated by centrifugation and washed repeatedly with absolute ethanol and ultrapure water. The final products were dried in an oven at 80 °C overnight. The samples were heated at 600 °C in air to remove surface fluoride impurities and denoted as Rut_111.

S3. Fourier transform infrared spectra of adsorbed pyridine (Pyridine-FTIR) and

temperature programmed desorption of NH$_3$ (NH$_3$-TPD) measurement.

The FTIR spectra of pyridine chemisorbed on the materials were obtained on a Thermo Nicolet iS50 spectrophotometer in the 1400-1650 cm^{-1} range. Samples were pretreated in situ, including preheating at 150 °C for 2 h, cooling to room temperature, and then equilibrating with pyridine for 30 min. Then the pyridine adsorbed sample was heated at 150 °C for 30 min, and FTIR spectra were record ed at 100 °C.

The NH$_3$-TPD measurements were performed as follows. 100 mg of the samples were pretreated in a helium (He) atmosphere at 500 °C for 1 h and then cooled to 100 °C. The NH$_3$ was adsorbed at 100 °C for 30 min until saturation, then purged with He gas at 100 °C to remove physically adsorbed NH$_3$. Desorption of NH$_3$ was carried out by increasing the temperature from 100 to 600 °C at a heating rate of 10 °C min^{-1} under constant He gas flow. The amount of NH$_3$ desorbed was measured using a thermal conductivity detector.

S4. Analysis of reaction kinetics data.

The 4-NP generation kinetics data were fitted to a least-squares model:

$$y_i = \frac{C_i}{C_F} = k_{obs} \cdot t_i + b \tag{1}$$

$$k_{obs} = \frac{n \cdot (\sum_{i=1}^{n} t_i \cdot y_i) - (\sum_{i=1}^{n} t_i) \cdot (\sum_{i=1}^{n} y_i)}{n \cdot (\sum_{i=1}^{n} t_i^2) - (\sum_{i=1}^{n} t_i)^2} \tag{2}$$

$$r = \frac{\sum_{i=1}^{n} t_i \cdot y_i - n \cdot \bar{t} \cdot \bar{y}}{\sqrt{(\sum_{i=1}^{n} t_i^2 - n \cdot (\bar{t})^2) \cdot (\sum_{i=1}^{n} y_i^2 - n(\bar{y})^2)}} \tag{3}$$

The points to be taken at intervals in this reaction system are (t_1, y_1), (t_2, y_2), ... (t_n, y_n). where C_i (mg L^{-1}) is the 4-NP concentration at reaction time t_i (h), C_F (mg L^{-1}) is the final 4-NP

concentration, k_{obs} (h^{-1}) is the apparent kinetics constant, b is the intercept of the line, $\bar{t}$ is the average of t_1 through t_n, $\bar{y}$ is the average of y_1 through y_n, and r is the correlation coefficient.

S5. Statistical analysis.

Paired Student's t-test, one-way ANOVA and the least significant difference (LSD) analysis were performed in the SPSS 22.0 software program for statistical analysis. A statistically significant difference was defined as a p-value less than 0.05.

S6. Density Functional Theory (DFT) calculation

In DFT calculation, adsorption model of pNPP was constructed based on anatase phase TiO_2 (001) 4×3×1, anatase phase TiO_2 (101) 2×4×1, rutile phase TiO_2 (110) 5×2×1 and rutile phase TiO_2 (111) 3×3×1 supercells. Structural optimization was performed by Vienna *Ab-initio* Simulation Package (VASP)[5] with the projector augmented wave (PAW) method.[6] The exchange-functional was treated using the Perdew-Burke-Ernzerhof (PBE)[7] functional. The DFT-D3 correction[8] was adopted to describe weak interactions between atoms. Cut-off energy of the plane-wave basis was set at 450 eV in structural optimization. For the optimization of both geometry and lattice size, the Brillouin zone integration was performed with a Monkhorst-Pack[9] k-point sampling of 0.04 $Å^{-1}$. Specifically, the k-point sampling was 2×2×1 for anatase phase TiO_2 (001), rutile phase TiO_2 (110), and rutile phase TiO_2 (111), and it was 1×2×1 for anatase phase TiO_2 (101). The self-consistent calculations applied a convergence energy threshold of 10^{-5} eV. The equilibrium geometries and lattice constants were optimized with maximum stress on each atom within 0.02 eV $Å^{-1}$. Spin polarization was adopted to describe the magnetism of pNPP adsorption model.

S7. Estimation the densities of surface active sites

The abundance of surface active sites for the materials was calculated from the surface area

concentrations (8 m^2 L^{-1}) of the different materials, the proportions of different exposed facets, and the densities of active sites (i.e., unsaturated Ti atoms[10]) on a given facet. The geometric models (insets of Fig. 1) of the nanomaterials were built using the WinXMorph software, based on the morphologies and sizes measured by scanning electron microscopy (SEM) and transmission electron microscopy (TEM) and the predominantly exposed facets identified based on the high-resolution TEM (HRTEM) and fast Fourier transform (FFT) results. Next, the proportions of different exposed facets were calculated for the materials,[2] according to the geometric models and the measured particle dimensions. The densities of active sites on a given facet (i.e., 5.1 and 7.0 sites nm^{-2} for the {101} and {001} facet of anatase, respectively) were obtained from the literature.[11] The estimated concentration of surface active sites in these materials are 4.1×10^{19} – 5.4×10^{19} L^{-1}, which are far higher than the initial concentration of pNPP or the total concentration of pNPP and orthophosphate ion at any time during the test (9.6×10^{18} molecules L^{-1}).

**Table S1** Surface chemistry properties of the TiO_2 nanomaterials determined by XPS

Material	Surface O (at%)	O (at%)			Surface Ti (at%)	O_{latt}/Ti ratio
		OH	H_2O	O_{latt}		
Ana_101	66.8	6.4	–	60.4	33.2	1.82
Ana_001	66.4	6.0	–	60.4	33.6	1.80
Rut_110	66.7	4.7	–	62.0	33.3	1.86
Rut_111	69.3	4.3	4.4	60.6	30.7	1.97

Table S2 Summary of the experimental parameters and fitted apparent rate constants of pNPP hydrolysis with initial pNPP concentration at 6.0 mg L^{-1}.

| Exp. No.	Catalyst	$C\_catalyst$ (m^2 L^{-1})	C_pNPP (mg L^{-1})	pH	Apparent kinetic constant	
					k_{obs} [a] (h^{-1})	r
1a	Blank	8.0	6.0	5.0	5.35×10^{-4}	0.619
1b	Ana_101	8.0	6.0	5.0	2.25×10^{-2}	0.965
1c	Ana_001	8.0	6.0	5.0	2.45×10^{-2}	0.884
1d	Rut_110	8.0	6.0	5.0	1.44×10^{-3}	0.888
1e	Rut_111	8.0	6.0	5.0	9.15×10^{-4}	0.862
2a	Blank	8.0	6.0	6.0	5.66×10^{-4}	0.810
2b	Ana_101	8.0	6.0	6.0	8.26×10^{-3}	0.903
2c	Ana_001	8.0	6.0	6.0	7.57×10^{-3}	0.860
2d	Rut_110	8.0	6.0	6.0	1.58×10^{-3}	0.953
2e	Rut_111	8.0	6.0	6.0	8.03×10^{-4}	0.890
3a	Blank	8.0	6.0	7.0	3.83×10^{-4}	0.971
3b	Ana_101	8.0	6.0	7.0	3.30×10^{-3}	0.932
3c	Ana_001	8.0	6.0	7.0	2.69×10^{-3}	0.949
3d	Rut_110	8.0	6.0	7.0	4.94×10^{-4}	0.926
3e	Rut_111	8.0	6.0	7.0	3.34×10^{-4}	0.778
4a	Blank	8.0	6.0	8.0	5.10×10^{-4}	0.978
4b	Ana_101	8.0	6.0	8.0	1.95×10^{-3}	0.976
4c	Ana_001	8.0	6.0	8.0	1.23×10^{-3}	0.973
4d	Rut_110	8.0	6.0	8.0	3.78×10^{-4}	0.954
4e	Rut_111	8.0	6.0	8.0	4.47×10^{-4}	0.946

[a] k_{obs} = apparent kinetic constant.
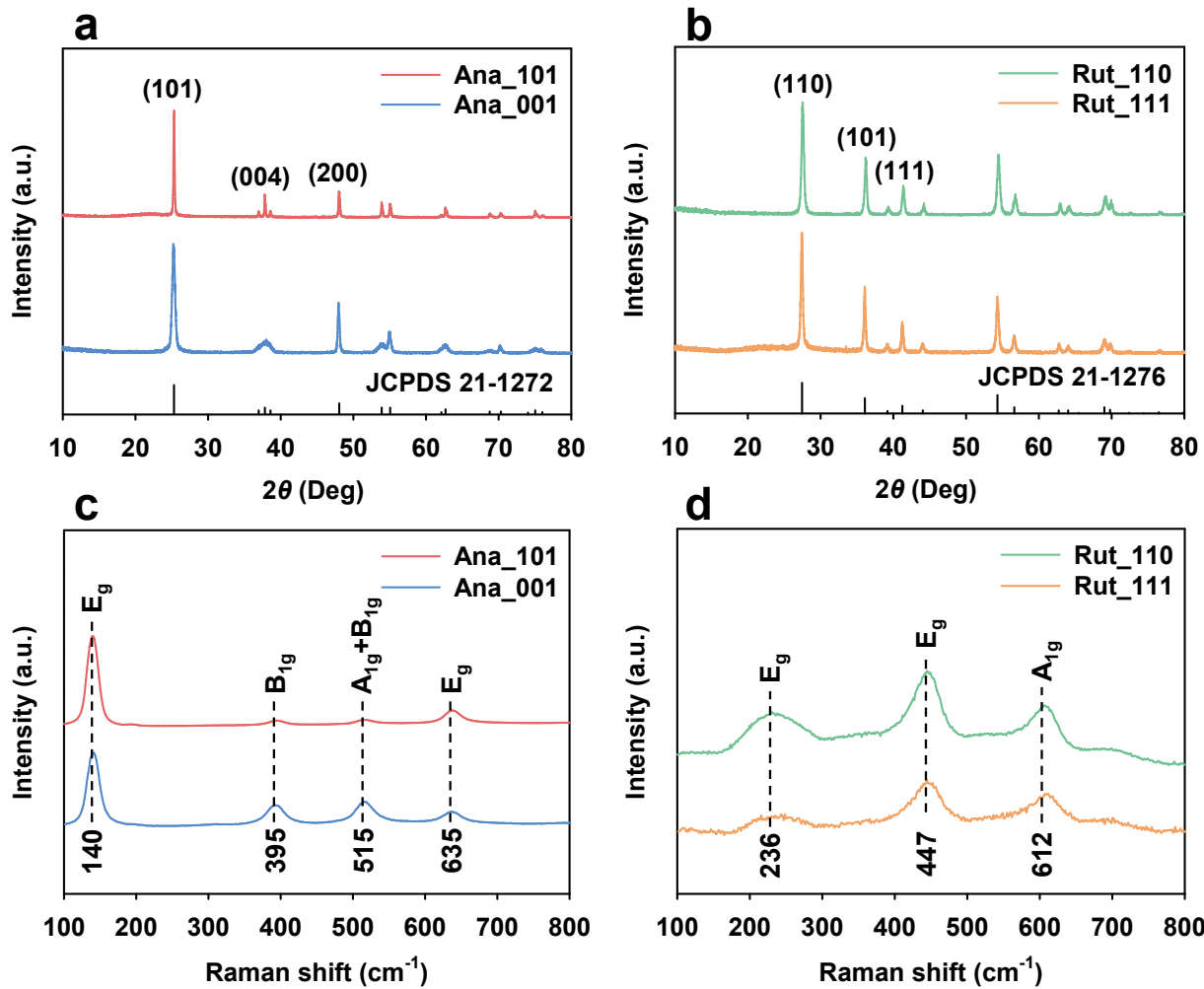
Fig. S1 X-ray diffraction (XRD) patterns and Raman spectra of anatase (a, c) and rutile (b, d) nanomaterials, respectively.
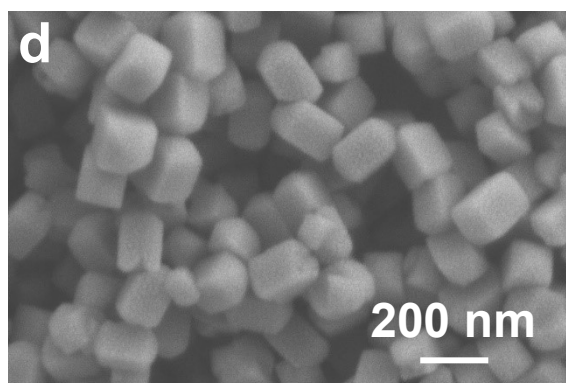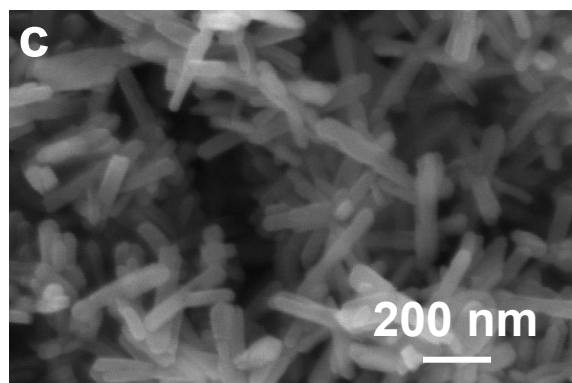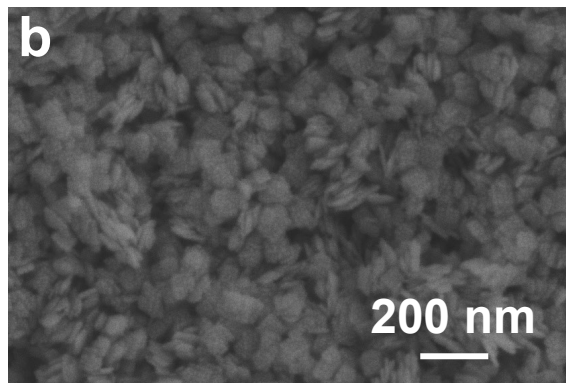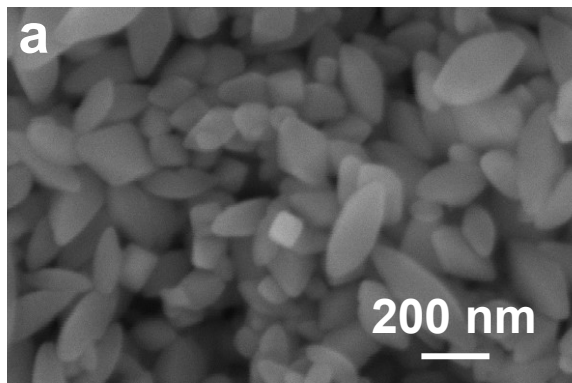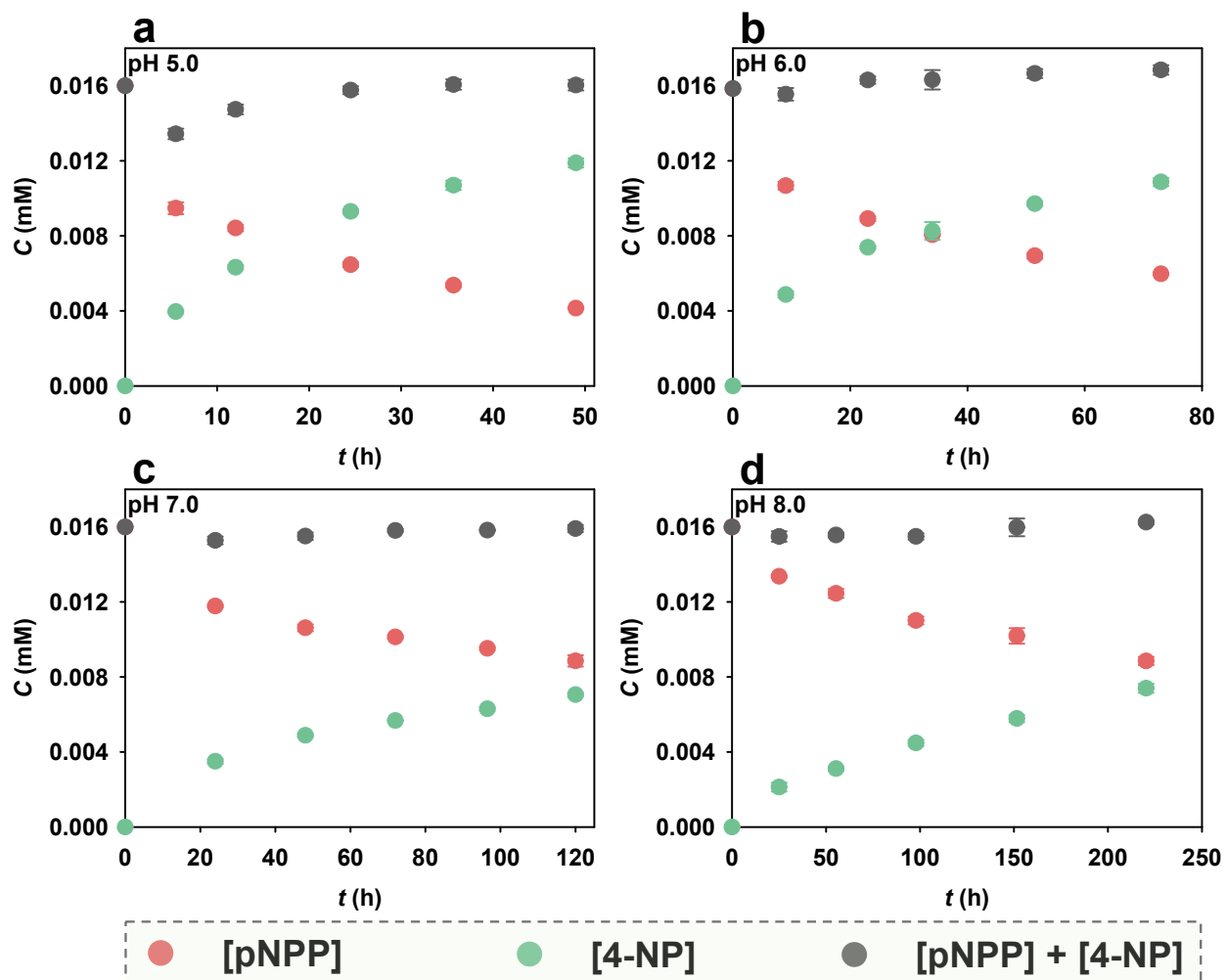
Fig. S2 Scanning electron microscopy (SEM) images of Ana_101 (a), Ana_001 (b), Rut_110 (c) and Rut_111 (d) nanomaterials.
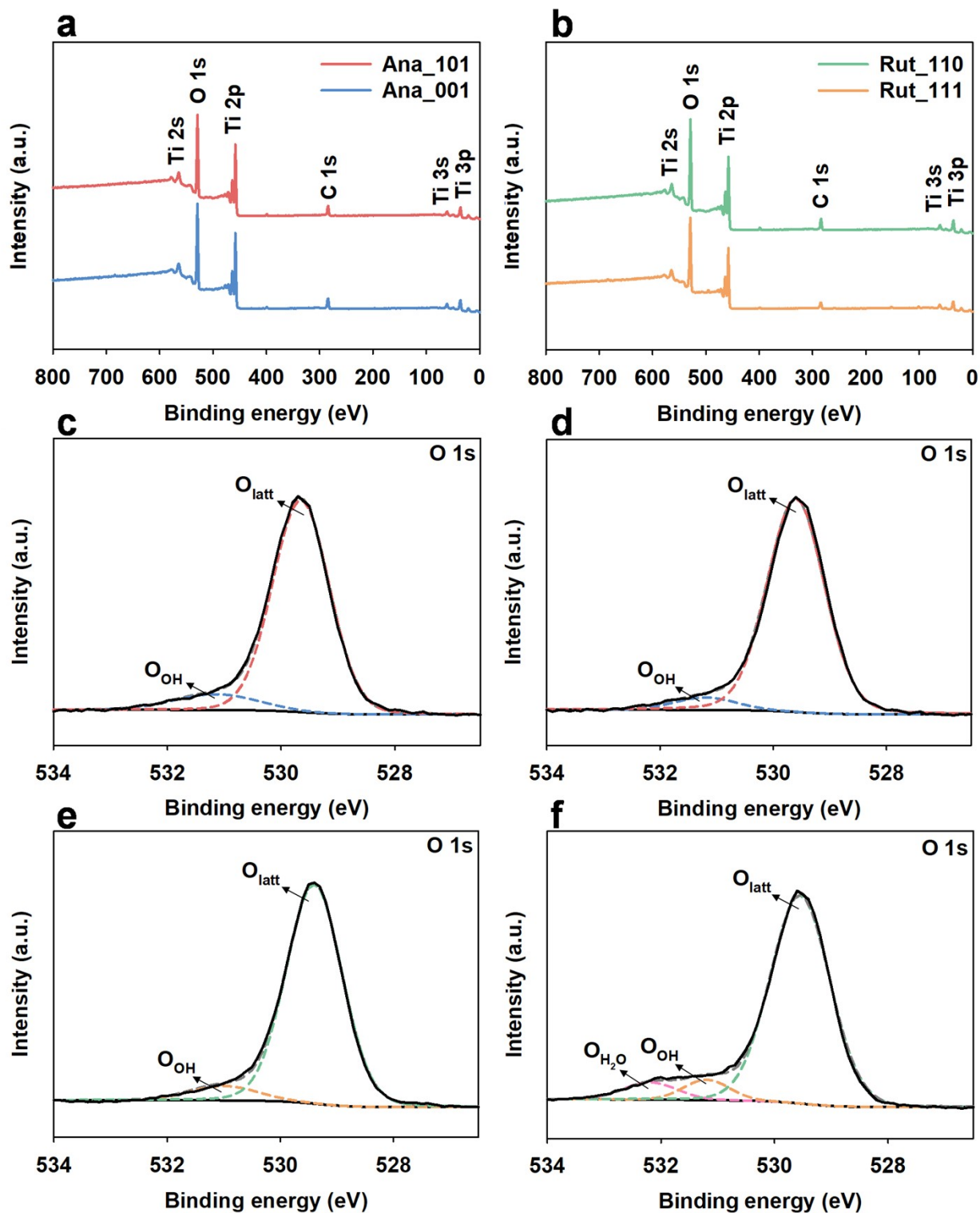
Fig. S3 XPS spectra of anatase (a) and rutile (b) nanomaterials. Curve fits of O 1s spectra of Ana_101 (c), Ana_001 (d), Rut_110 (e) and Rut_111 (f) nanomaterials.
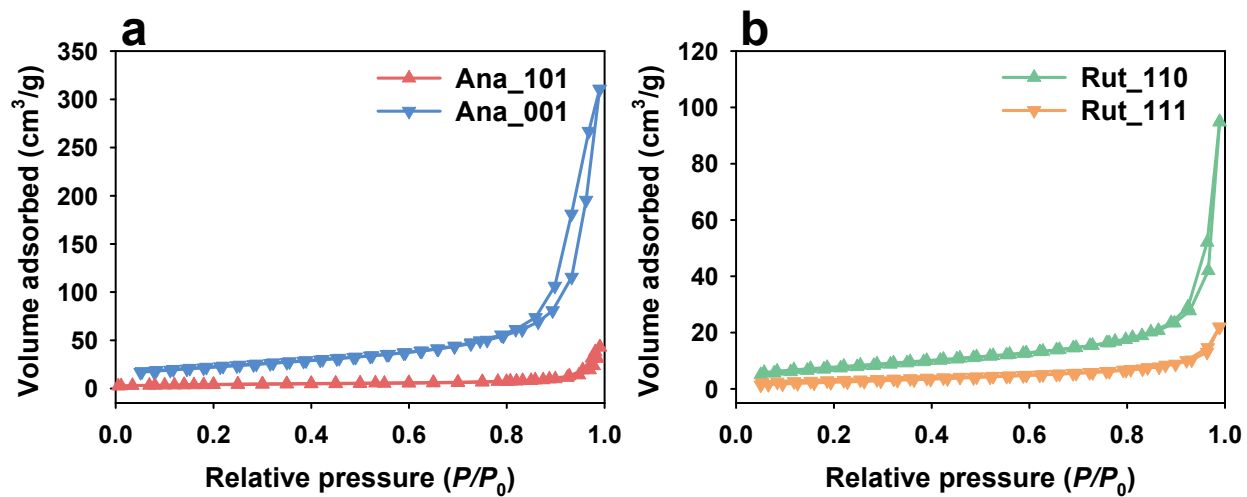
**Fig. S4.** The N$_2$ adsorption–desorption isotherms of anatase (a) and rutile (b) nanomaterials, respectively.

Fig. S5 Changes of pNPP and 4-NP concentrations during pNPP hydrolysis experiments in aqueous suspensions of Ana_101 at pH 5.0 (a), 6.0 (b), 7.0 (c) and 8.0 (d), respectively.
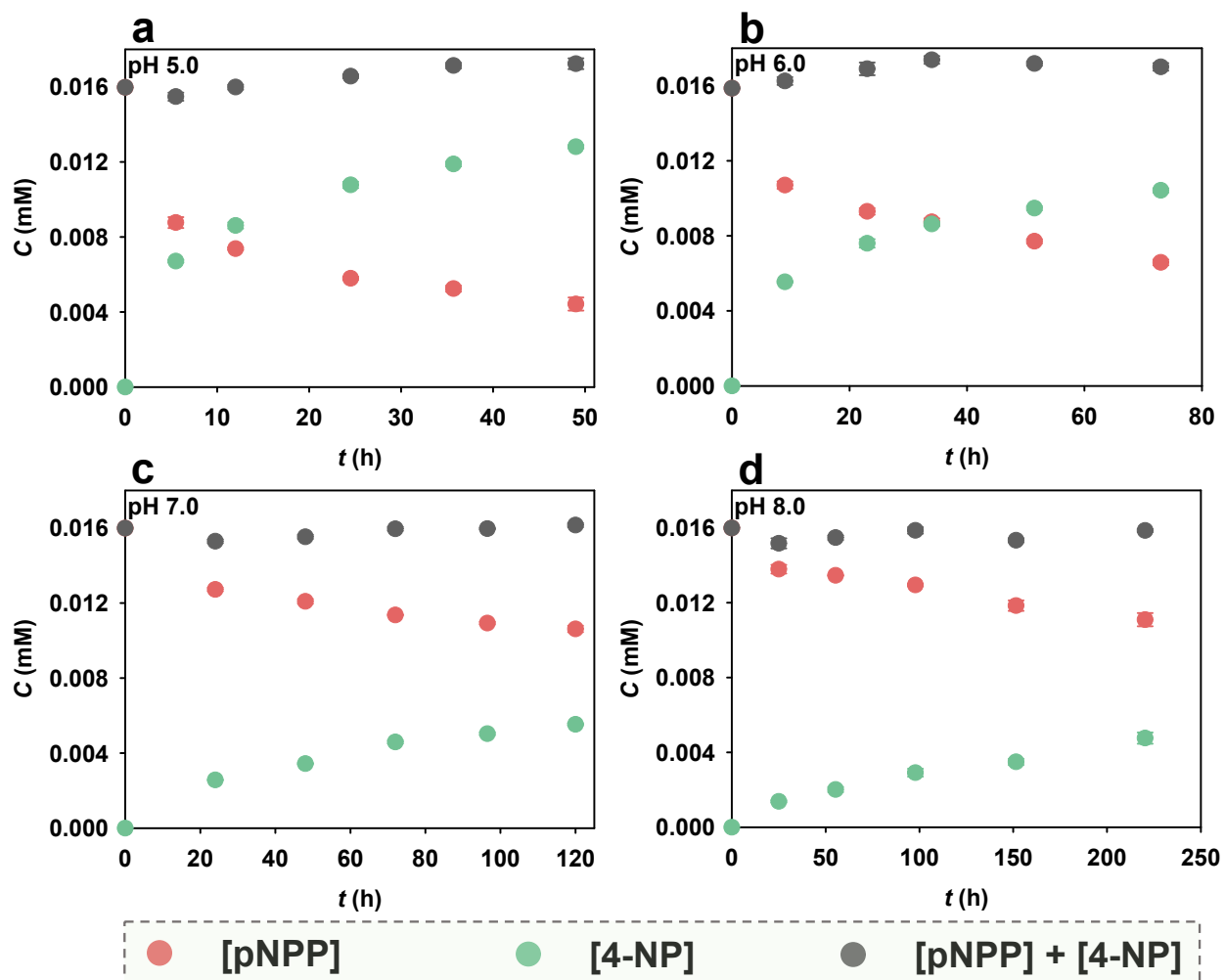
Fig. S6 Changes of pNPP and 4-NP concentrations during pNPP hydrolysis experiments in aqueous suspensions of Ana_001 at pH 5.0 (a), 6.0 (b), 7.0 (c) and 8.0 (d), respectively.
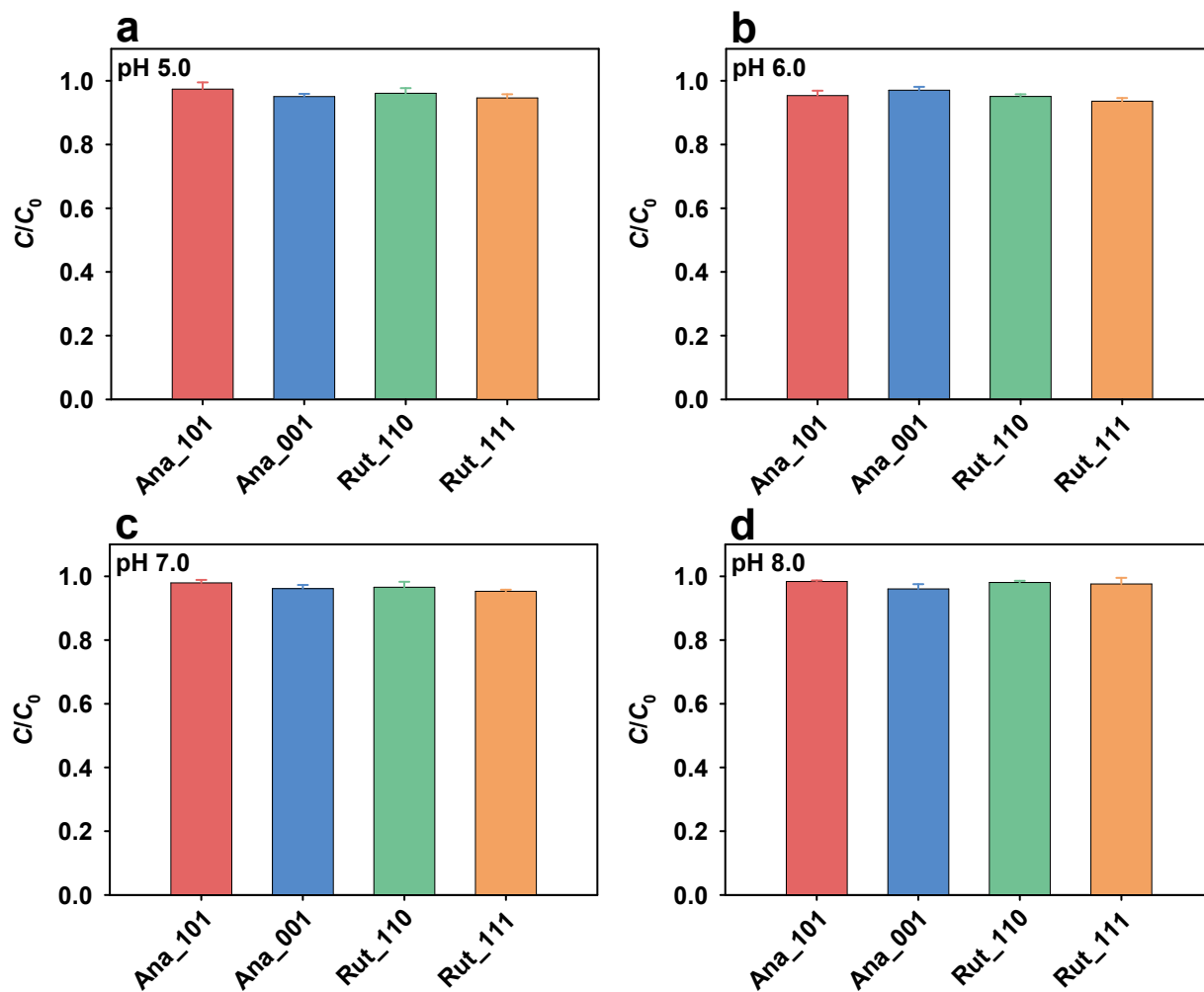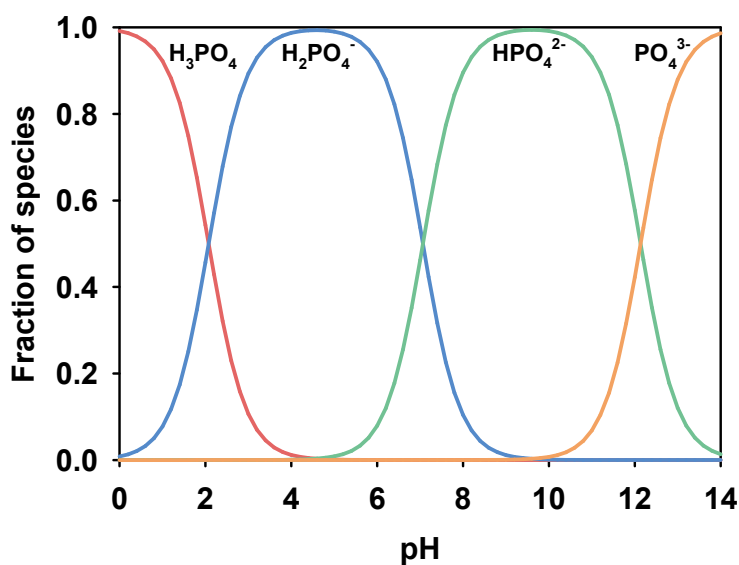
Fig. S7 Adsorption of 4-NP on anatase and rutile nanomaterials at different pH values: (a) 5.0, (b) 6.0, (c) 7.0, and (d) 8.0. The error bars represent standard deviations of triplicate samples.
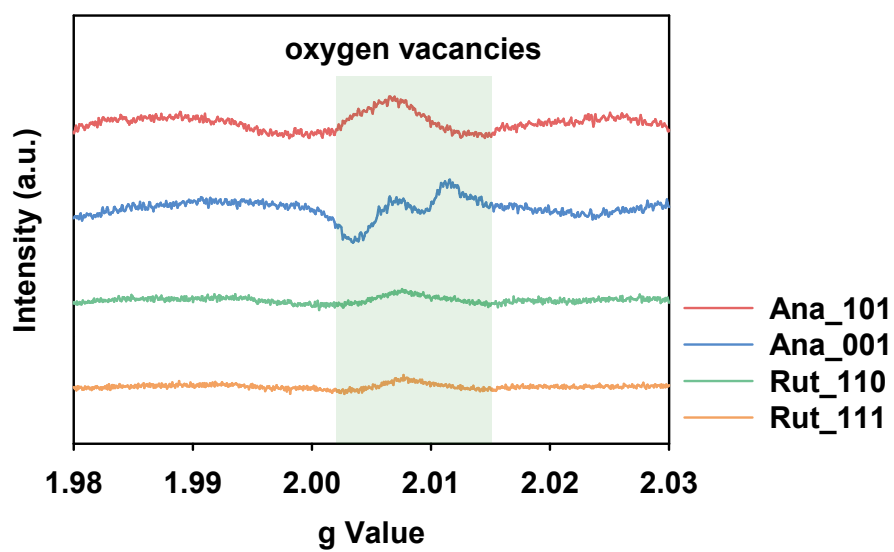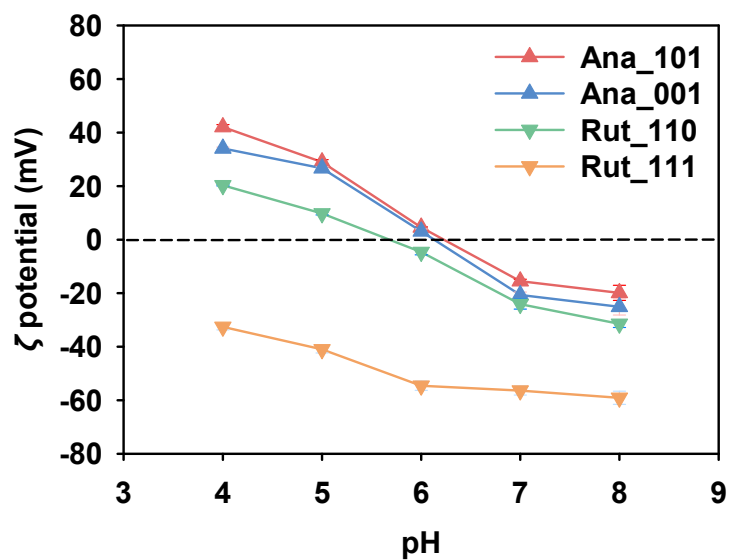
**Fig. S8** EPR spectra of the different TiO$_2$ nanomaterials.

Fig. S9 Speciation of orthophosphate ions in aqueous solution. The speciation data were calculated based on the pK_a values of $pK_{a1} = 2.12$, $pK_{a2} = 7.2$, $pK_{a3} = 12.36$.[12] The activity coefficients for the deprotonated species $H_2PO_4^-$, HPO_4^{2-} and PO_4^{3-} were estimated to be 0.90, 0.66 and 0.39, respectively, for an ionic strength of 10 mM, according to the Davies Equation.

Fig. S10 The ζ potential values of different TiO_2 nanomaterials at different pH.
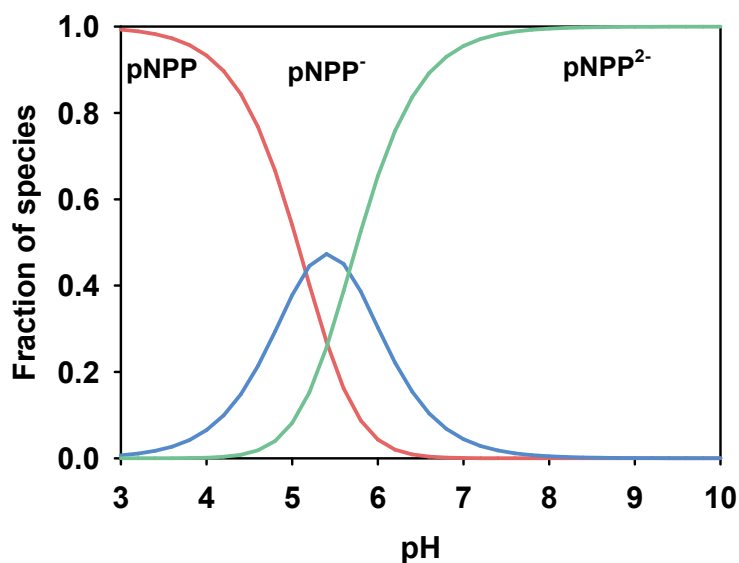
Fig. S11 Speciation of pNPP in aqueous solution. The speciation data were calculated based on the pK_a values of $pK_{a1} = 5.2$, $pK_{a2} = 5.8$.[13] The activity coefficients for the deprotonated species pNPP$^-$ and pNPP^{2-} were estimated to be 0.90 and 0.66, respectively, for an ionic strength of 10 mM, according to the Davies Equation.

References

1. T. Li, Z. L. Shen, Y. L. Shu, X. G. Li, C. J. Jiang and W. Chen, Facet-dependent evolution of surface defects in anatase TiO_2 by thermal treatment: implications for environmental applications of photocatalysis, *Environ. Sci.: Nano*, 2019, **6**, 1740-1753.

2. Z. L. Shen, Z. H. Zhang, T. Li, Q. Q. Yao, T. Zhang and W. Chen, Facet-dependent adsorption and fractionation of natural organic matter on crystalline metal oxide nanoparticles, *Environ. Sci. Technol.*, 2020, **54**, 8622-8631.

3. R. F. Chong, J. Li, X. Zhou, Y. Ma, J. X. Yang, L. Huang, H. X. Han, F. X. Zhang and C. Li, Selective photocatalytic conversion of glycerol to hydroxyacetaldehyde in aqueous solution on facet tuned TiO_2-based catalysts, *Chem. Commun.*, 2014, **50**, 165-167.

4. B. Fu, Z. J. Wu, K. Guo and L. Y. Piao, Rutile TiO_2 single crystals delivering enhanced photocatalytic oxygen evolution performance, *Nanoscale*, 2021, **13**, 8591-8599.

5. J. Hafner, *Ab-initio* simulations of materials using VASP: density-functional theory and beyond, *J. Comput. Chem.*, 2008, **29**, 2044-2078.

6. P. E. Blöchl, Projected augmented-wave method, *Phys. Rev. B*, 1994, **50**, 17953.

7. J. P. Perdew, K. Burke and M. Ernzerhof, Generalized gradient approximation made simple, *Phys. Rev. Lett.*, 1996, **77**, 3865-3868.

8. S. Grimme, Semiempirical GGA-type density functional constructed with a long-range dispersion correction, *J. Comput. Chem.*, 2006, **27**, 1787-1799.

9. H. J. Monkhorst and J. D. Pack, Special points for Brillouin-zone integrations, *Phys. Rev. B*, 1976, **13**, 5188-5192.

10. L. Yan, J. J. Du and C. Y. Jing, How TiO_2 facets determine arsenic adsorption and photooxidation: spectroscopic and DFT studies, *Catal. Sci. Technol.*, 2016, **6**, 2419-2426.

11. M. Lazzeri, A. Vittadini and A. Selloni, Structure and energetics of stoichiometric TiO_2 anatase surfaces, *Phys. Rev. B*, 2001, **63**, 155409.

12. X. Y. Hong, S. D. Zhu, M. Z. Xia, P. Du and F. Y. Wang, Investigation of the efficient adsorption performance and adsorption mechanism of 3D composite structure La nanosphere-coated Mn/Fe layered double hydrotalcite on phosphate, *J. Colloid Interface*

Sci., 2022, **614**, 478-488.

13. M. Li, R. L. Harbron, J. V. M. Weaver, B. P. Binks and S. Mann, Electrostatically gated membrane permeability in inorganic protocells, *Nat. Chem.*, 2013, **5**, 529-536.